nature materials

SUPPLEMENTARY INFORMATION

https://doi.org/10.1038/s41563-019-0452-y

In the format provided by the authors and unedited.

Programming shape using kirigami tessellations

Gary P. T. Choi[1], Levi H. Dudte[1] and L. Mahadevan[1,2,3]*

[1]John A. Paulson School of Engineering and Applied Sciences, Harvard University, Cambridge, MA, USA. [2]Departments of Physics, and Organismic and Evolutionary Biology, Harvard University, Cambridge, MA, USA. [3]Kavli Institute for Nanobio Science and Technology, Harvard University, Cambridge, MA, USA. *e-mail: lmahadev@g.harvard.edu

Supplementary information for "Programming shape using kirigami tessellations"

Gary P. T. Choi, Levi H. Dudte, L. Mahadevan

Contents

1 Deployable planar tessellations

In the main text we focused on generalized kirigami patterns derived from the quad kirigami tessellations. Here, we consider a wider range of deployable planar tessellations.

It is well known that the only regular polygons that can tile the plane are triangle, square and hexagon. In fact, all of them can be used to produce deployable planar tessellations, such that the deployed configurations of them also tile the plane.

The triangle kirigami tessellation, also known as the kagome tessellation, is a floppy auxetic pattern with six triangles surrounding a single node. As shown in Figure S1**a**, by introducing cuts along the six edges incident to every interior node, we can make the triangle tessellation deployable.

As introduced in the main text, the quad kirigami tessellation is a four-fold auxetic pattern with four quads surrounding a single node. As shown in Figure S1**b**, by introducing cuts along the four edges incident to every interior node, we can make the quad tessellation deployable.

The design of a deployable hexagon tessellation is slightly different. While hexagons can tile the plane, it is impossible to simply introduce cuts along their edges to form a deployable pattern. The reason is that all interior nodes of a regular hexagonal tiling are of degree 3, and hence no matter how cuts are introduced along the three edges incident to a node, the faces will either become fully disconnected or not deployable. One way to design a deployable hexagon tessellation is to leave one hexagonal hole surrounded by six regular hexagonal faces. With the introduction of such holes, it becomes possible for us to introduce cuts along the edges alternatively to get a deployable hexagon tessellation, as illustrated in Figure S1**c**.

Besides the deployable tessellations based on regular polygons, we can also generalize more complex multiple-cell deployable tessellations using our approach. We consider two multiple-cell kirigami patterns derived from Islamic decorative tilings [1], as shown in Figure S1**d**,**e**. Both patterns have unique, singular deployed configurations.

To simplify the computation, we only consider kirigami tessellations which are rectangular. In other words, the tessellations are formed by duplicating one of the unit cells shown in Figure S1 by $m \times n$ times, where m is the number of duplications along the horizontal direction and n is the number of duplications along the vertical direction.

2 Constrained optimization in the deployed space

Denote the fully deployed configuration of a standard kirigami pattern by $\mathcal{D}$, and the target boundary shape together with its interior by $\mathcal{S}$. Our inverse design approach produces a generalized kirigami pattern that approximates ∂S upon deployment by suitably deforming $\mathcal{D}$, and the key step is to solve a constrained optimization problem. In the main text, we discussed the formulation of the constrained optimization problem with a focus on the quad kirigami pattern. Here, we discuss the formulations with the other base patterns that we mentioned above.

Note that the objective function, the boundary shape matching constraints and the non-overlap constraints are the same for all base tessellations. Readers are referred to the main text for a description of them. Below, we focus on the contractibility constraints and the extra constraints.

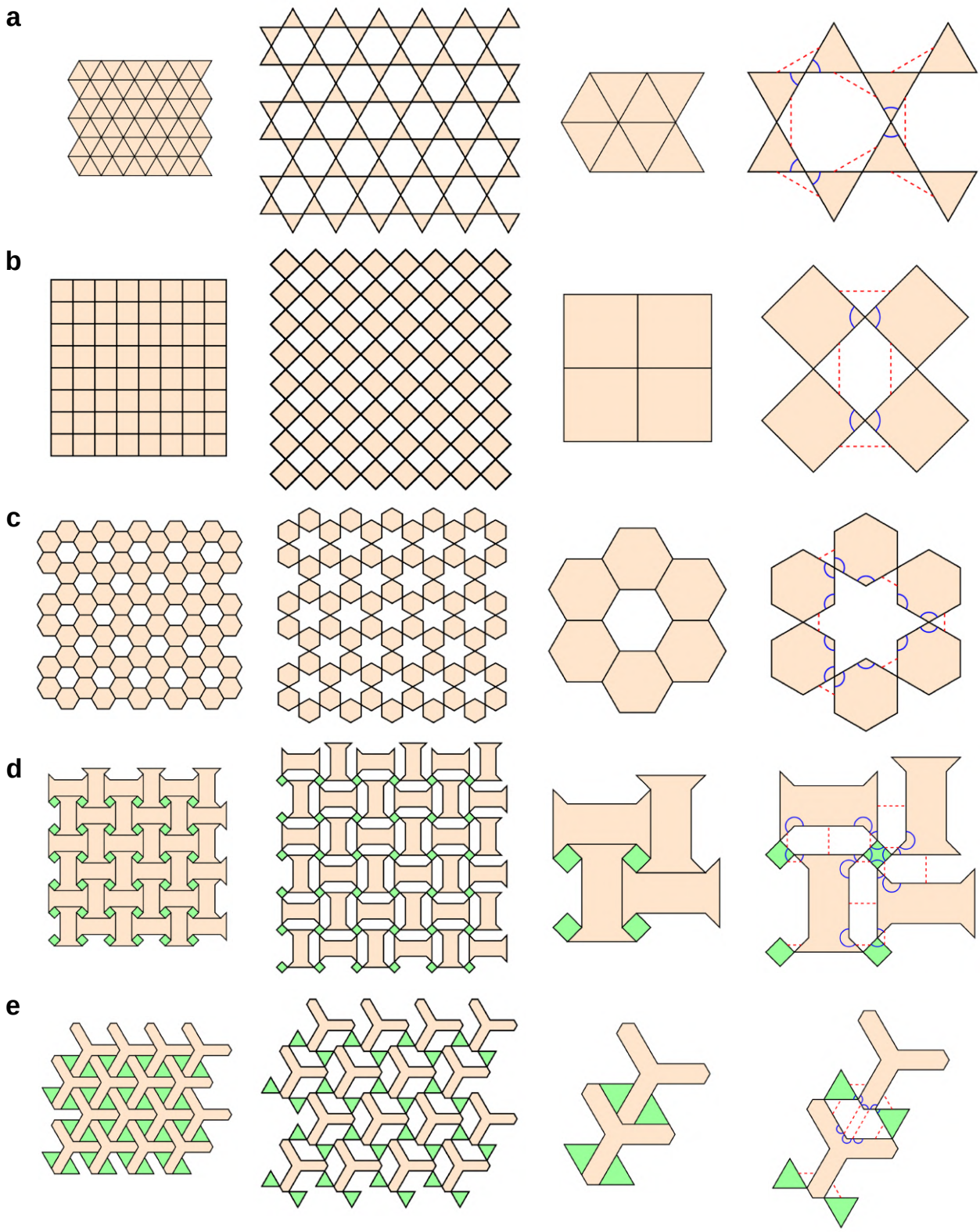

Figure S1: **Five deployable patterns that we consider. a**, A triangle kirigami tessellation. **b**, A quad kirigami tessellation. **c**, A hexagon kirigami tessellation. **d**,**e**, Two multiple-cell Islamic kirigami tessellations. Corresponding edge pairs are connected by red dotted lines, and angles involved in the angle constraints are highlighted in blue.

2.1 Contractibility constraints for different generalized kirigami patterns

2.1.1 Generalized kirigami patterns derived from planar tessellations without holes

For the generalized triangle and multiple-cell Islamic kirigami patterns, the contractibility constraints are the same as the ones for the quad pattern. More specifically, for a valid deployed configuration of a generalized kirigami pattern derived from such tessellations, the following two *contractibility* constraints should be satisfied in the deployed space:

(i) *Edge length* constraints: For every pair of edges with edge lengths a, b in the deployed space that correspond to the same cut, we should have

$$a^2 - b^2 = 0. \tag{S1}$$

The edge pairs are connected by red dotted lines in Figure S1.

(ii) *Angle sum* constraints: For every set of angles in the deployed space that correspond to an interior node, their sum should be 2π:

$$\sum_i \theta_i = 2\pi, \tag{S2}$$

where θ_i are angles in the deployed space highlighted in blue in Figure S1.

2.1.2 Generalized kirigami patterns derived from planar tessellations with holes

For generalized kirigami patterns derived from base patterns with holes, such as the hexagon kirigami pattern in Figure S1**c**, the contractibility constraints are slightly different. For the hexagon kirigami pattern, we have the following contractibility constraints:

(i) *Edge length* constraints: For every pair of edges with length a, b in the deployed space that correspond to the same cut, we should have

$$a^2 - b^2 = 0. \tag{S3}$$

The edge pairs are connected by red dotted lines in Figure S1**c**.

(ii) *One-ring angle sum* constraints: For the hexagon kirigami pattern, every hexagonal hole is surrounded by six hexagons. As the angle sum of an n-sided polygon is $(n-2)\pi$, the six angles of the hexagonal hole should add up to 4π. Note that the explementary angles of them can be expressed using the twelve angles in the hexagonal one-ring highlighted in blue in Figure S1**c**. Therefore, in a valid deployed configuration of a generalized hexagon kirigami pattern, we should have

$$6 \times 2\pi - \sum_{i=1}^{12} \theta_i = 4\pi \Leftrightarrow \sum_{i=1}^{12} \theta_i = 8\pi, \tag{S4}$$

where θ_i are the angles in the deployed space highlighted in blue in Figure S1**c**.

(iii) *Diagonal consistency* constraints: The ring angle sum constraints are insufficient to guarantee that the one-ring hexagonal faces form a closed loop, as there is no control on the edge lengths of the hexagonal holes. To ensure the closed loop condition, we impose

the diagonal consistency constraints which involve the edge lengths of the hexagonal holes. As depicted in Figure S2, at every hole enclosed by six hexagonal faces, we should have

$$\begin{cases} d_1^2 - d_2^2 = 0, \\ d_3^2 - d_4^2 = 0, \\ d_5^2 - d_6^2 = 0, \end{cases} \tag{S5}$$

where each pair $\{d_1, d_2\}$, $\{d_3, d_4\}$, $\{d_5, d_6\}$ refers to a diagonal of the hole calculated in two ways. More explicitly, we have

$$d_i^2 = \left(a_i - \frac{b_i \sin \nu_i}{\sin(\mu_i+\nu_i)}\right)^2 + \left(c_i - \frac{c_i \sin \mu_i}{\sin(\mu_i+\nu_i)}\right)^2 + 2\left(a_i - \frac{b_i \sin \nu_i}{\sin(\mu_i+\nu_i)}\right)\left(c_i - \frac{c_i \sin \mu_i}{\sin(\mu_i+\nu_i)}\right)\cos(\mu_i + \nu_i), \tag{S6}$$

where

$$\mu_i = 2\pi - \gamma_i - \eta_i \tag{S7}$$

and

$$\nu_i = 2\pi - \phi_i - \psi_i. \tag{S8}$$

Note that all the edge lengths a_i, b_i, c_i and the angles $\gamma_i, \eta_i, \phi_i, \psi_i$ are information in the deployed space. Therefore, the diagonal consistency constraints can be imposed in our constrained optimization problem, which takes place in the deployed space.

While the above constraints are discussed in the setting of hexagon kirigami patterns, similar constraints can be established for other kirigami patterns with holes.

2.2 Extra constraints for achieving different effects

Besides the boundary shape matching constraints, the contractibility constraints and the non-overlap constraints, we can impose extra constraints to further control the shape of the generalize kirigami patterns. Below, we discuss a number of possible extra constraints for each tessellation, which lead to different interesting effects on the resulting generalized kirigami patterns.

2.2.1 Regular boundary angle sum constraints for generalized kagome kirigami patterns

We consider enforcing the generalized kagome patterns to be a rectangle up to a small zig-zag effect on the left and the right boundaries, at which the angle sum is desired to be a multiple of $\pi/3$. To achieve this, we impose the following *regular boundary angle sum* constraints. For each boundary node, we denote the number of faces adjacent to it by k and the angles by $\zeta_1, \zeta_2, \ldots, \zeta_k$. We enforce

$$\sum_{i=1}^{k} \zeta_i = \frac{k\pi}{3}. \tag{S9}$$

In other words, the angle sum at the top and the bottom boundary nodes is π, and the angle sum at the left and the right boundary nodes is either $2\pi/3$ or $4\pi/3$. The two corner nodes on the left will have angle sum $2\pi/3$, and the two corner nodes on the right will have angle $\pi/3$.

2.2.2 Rectangular and square boundary constraints for generalized quad kirigami patterns

As mentioned in the main text, we can enforce the boundary of the generalized quad kirigami pattern to be either a rectangle or even a square. To achieve this, we impose the following extra constraints:

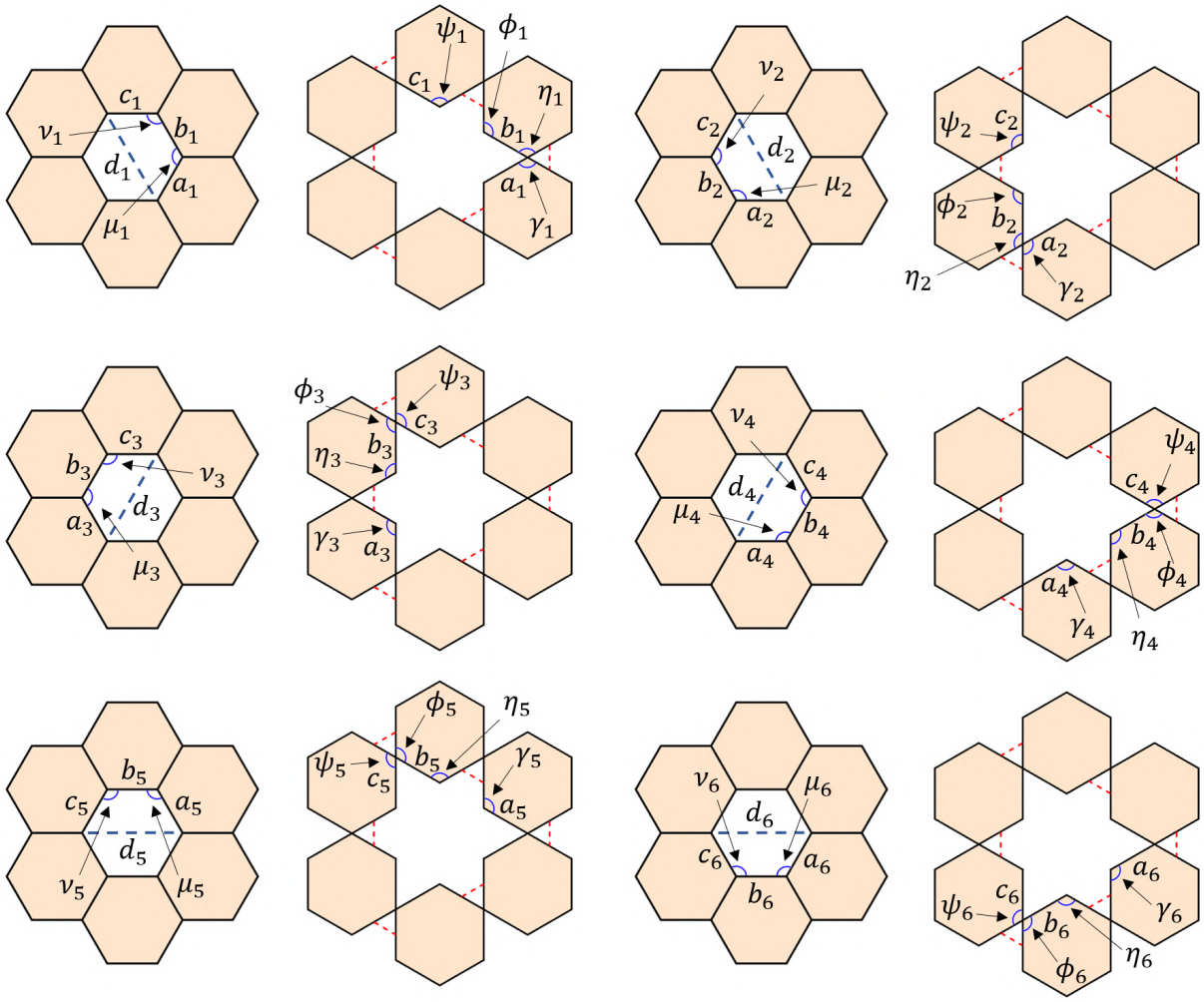

Figure S2: **An illustration of the diagonal consistency constraints for the generalized hexagon kirigami patterns.** Each row shows how the length of a diagonal of the hexagonal hole can be calculated in two ways using the angles and edge lengths in the deployed space.

(i) *Boundary angle* constraints: For every set of two angles ζ_1, ζ_2 in the deployed configuration that correspond to the same boundary node in the kirigami pattern, we enforce

$$\zeta_1 + \zeta_2 = \pi. \tag{S10}$$

For the four angles ξ_1, ξ_2, ξ_3, ξ_4 in the deployed configuration that correspond to four corner angles in the kirigami pattern, we enforce

$$\xi_1 = \xi_2 = \xi_3 = \xi_4 = \frac{\pi}{2}. \tag{S11}$$

These constraints ensure that the deployed configuration corresponds to a rectangular generalized kirigami pattern.

(ii) *Equal boundary length* constraints: On top of the above constraints, we can further enforce the width and the height of the generalized kirigami pattern to be equal in length, making a square generalized kirigami pattern. To achieve this, denote the edges in the deployed configuration which correspond to the top boundary edges in the kirigami pattern by $\vec{e}_{T_i}$, $i = 1, \ldots, m$, and those in the deployed configuration which correspond to the right boundary edges in the kirigami pattern by $\vec{e}_{R_j}$, $j = 1, \ldots, n$. We enforce

$$\|\vec{e}_{T_1}\| + \|\vec{e}_{T_2}\| + \cdots + \|\vec{e}_{T_m}\| = \|\vec{e}_{R_1}\| + \|\vec{e}_{R_2}\| + \cdots + \|\vec{e}_{R_n}\|. \tag{S12}$$

2.2.3 Regular angle constraints for generalized hexagon kirigami patterns

For the generalized hexgaon kirigami patterns, we consider further regularizing their shapes by enforcing the following *regular angle* constraints. For each angle θ in the deployed configuration, we enforce

$$\theta = \frac{2\pi}{3}. \tag{S13}$$

Note that the choice of $2\pi/3$ is compatible with the one-ring angle sum constraints (S4). Even with such restrictions on all angles, we are able to obtain generalized hexagon kirigami patterns that match different shapes upon deployment.

2.2.4 Regular shape constraints for generalized multiple-cell Islamic kirigami patterns

Because of the more complicated geometry of the faces in the multiple-cell Islamic patterns, we impose a few extra constraints to regularize the shape of the generalized kirigami patterns produced.

(i) *Non-self-intersecting* constraints: Unlike the triangle, quad and hexagon patterns, the two multiple-cell Islamic patterns involve polygonal faces which are thinner and with a larger number of sides. To avoid those faces from having self-intersection, we can enforce inequality constraints similar to the non-overlap constraints introduced in the main text. In this case, we use the nodes on such faces to form vectors and enforce that the cross product is consistent with the face normal.

(ii) *Regular angle* constraints:

(a) For the four-fold Islamic pattern shown in Figure S1**d**, note that it contains four sharp corners for each I-shaped face. To avoid the corners from being squeezed in the generalized four-fold Islamic kirigami patterns, for each of such angles θ in the deployed space we enforce that

$$\theta = \frac{\pi}{4}. \tag{S14}$$

(b) For the hex Islamic pattern shown in Figure S1**e**, we note that each of the longer sides consists of three nodes, which form an angle of π. To preserve this feature in the generalized hex Islamic kirigami pattern, we enforce that all such straight lines in the deployed configuration of the generalized patterns remain to be straight lines, i.e. the angle sum equals π. Also, note that for this pattern there is no control on the boundary angles. To regularize them, we enforce that all the boundary angles remain unchanged in the deployed configuration of the generalized patterns.

2.3 Initial guess in the deployed space

Note that an initial guess in the deployed space is needed for solving the constrained optimization problem. There are many available options for the initial guess, and below are four choices that we consider in our work.

(i) **Standard deployed configuration**: The standard fully deployed configuration $\mathcal{D}$ of a regular kirigami pattern can be used as an initial guess. Note that it automatically satisfies the contractibility constraints. However, note that the boundary of it is usually very different from the target boundary curve ∂S.

(ii) **Standard deployed configuration with rescaling**: One can also consider suitably rescaling $\mathcal{D}$ according to ∂S so as to reduce the boundary mismatch error. Again, the rescaled configuration satisfies the contractibility constraints, but the boundary mismatch error is still nonzero in general.

(iii) **Conformal map**: We can apply the Schwarz-Christoffel map to produce a non-rigid transformation of $\mathcal{D}$ such that its boundary matches ∂S well. The angles in all faces are also well preserved under the conformal map. However, the edge length mismatch error is large in general.

(iv) **Quasi-conformal map**: We combine recent advances in conformal parameterization [2, 3] to obtain a conformal map $g : \mathcal{S} \to \mathcal{R}$ from $\mathcal{S}$ to a rectangle $\mathcal{R}$, and consider a rescaling transformation $h : \mathcal{R} \to \mathcal{D}$ to achieve the height and width of $\mathcal{D}$. The map $f = (h \circ g)^{-1} : \mathcal{D} \to \mathcal{S}$ is then a quasi-conformal mapping, with $f|_{\partial D} = \partial S$. Because of the rescaling transformation h, all angles will be distorted uniformly under f. Nevertheless, in general the distortion in edge lengths is smaller than that of the conformal map.

2.4 Contraction

To get the generalized kirigami pattern from the deployed configuration, we note that there is a 1-1 correspondence between every face in the pattern space and every face in the deployed space, with each pair of corresponding faces being identical up to translation and rotation. Therefore, we can simply begin from one face, and subsequently rotate and translate the adjacent faces in the deployed configuration to close up the gaps between the edges which correspond to the same cut. After all faces are rotated and translated, we get the generalized kirigami pattern that corresponds to the deployed configuration we obtained in the constrained optimization problem.

3 Implementation

Let $\mathbf{x}_1, \mathbf{x}_2, \ldots, \mathbf{x}_N$ be the coordinates of the nodes in the deployed space. The constrained optimization problem with the objective function, the boundary matching constraints, the contractibility constraints and the non-overlap constraints can be solved using `fmincon` in MATLAB, which minimizes the following Lagrangian via gradient descent:

$$\begin{aligned} &L(\mathbf{x}_1, \mathbf{x}_2, \ldots, \mathbf{x}_N, \lambda_{\text{boundary}}, \lambda_{\text{length}}, \lambda_{\text{angle}}, \lambda_{\text{non-overlap}}) \\ =&\frac{1}{M}\sum_{i=1}^{M}\left(\sum_j(\alpha_{i_j}-\beta_{i_j})^2+\sum_k(a_{i_k}-b_{i_k})^2\right)+\lambda_{\text{boundary}}\sum_i\|\mathbf{p}_i-\widetilde{\mathbf{p}}_i\|^2 \\ &+\lambda_{\text{length}}\sum(a^2-b^2)+\lambda_{\text{angle}}\sum(\sum\theta_i-2\pi)+\lambda_{\text{non-overlap}}\sum\langle(\mathbf{b}-\mathbf{a})\times(\mathbf{c}-\mathbf{a}),\vec{n}\rangle. \end{aligned} \tag{S15}$$

The minimizers $\mathbf{x}_1, \mathbf{x}_2, \ldots, \mathbf{x}_N$ then form a valid deployed configuration of a generalized kirigami pattern. In case there are additional constraints to be satisfied, we can also easily include them in the above Lagrangian.

Note that the objective function and all constraints can be expressed solely in terms of the $2N$ coordinates of the nodes $\mathbf{x}_1 = (x_1, y_1), \mathbf{x}_2 = (x_2, y_2), \ldots, \mathbf{x}_N = (x_N, y_N)$. To accelerate the computation, we supply the derivatives of the objective function and all constraints using the `SpecifyObjectiveGradient` and `SpecifyConstraintGradient` options in `fmincon`. It is easy to see that all the derivatives have a simple closed form in terms of the $2N$ variables $x_1, \ldots, x_N, y_1, \ldots, y_N$.

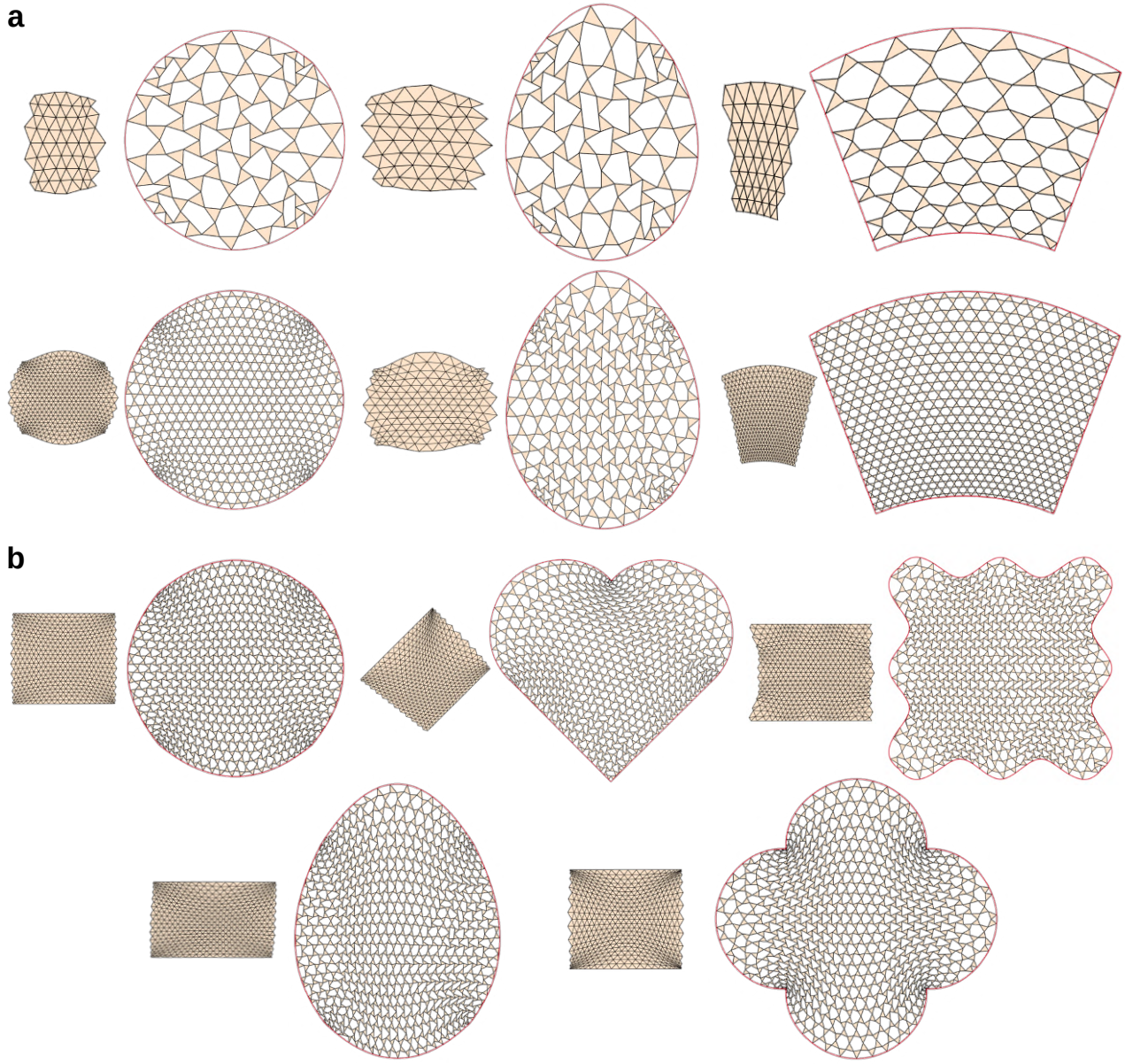

Figure S3: **Generalized kagome kirigami patterns. a**, Generalized kagome kirigami patterns with different target boundary shapes and different resolutions obtained by our approach. **b**, The results with the extra regular boundary angle sum constraints described in Section 2.2.1.

4 Results

Figure S3, Figure S4, Figure S5 and Figure S6 show respectively various generalized kirigami patterns obtained by our inverse design approach with the triangle, quad, hexagon and multiple-cell Islamic tessellations. It can be observed that our inverse design approach is capable of producing generalized kirigami patterns that deploy and approximate a wide range of shapes, possibly with different curvature properties or even sharp corners. Besides, the extra constraints that we introduced above can be effectively imposed in the constrained optimization problem to achieve a large variety of additional effects on the shape of the generalized kirigami patterns.

The constrained optimization problem is in general underconstrained and hence different initial guesses can lead to different valid deployed configurations of generalized kirigami patterns. Figure S7 shows the results obtained with four different initial guesses, including the standard deployed configuration of the quad kirigami pattern, the standard deployed configuration with rescaling, a conformal map of the standard deployed configuration and a quasi-conformal map of

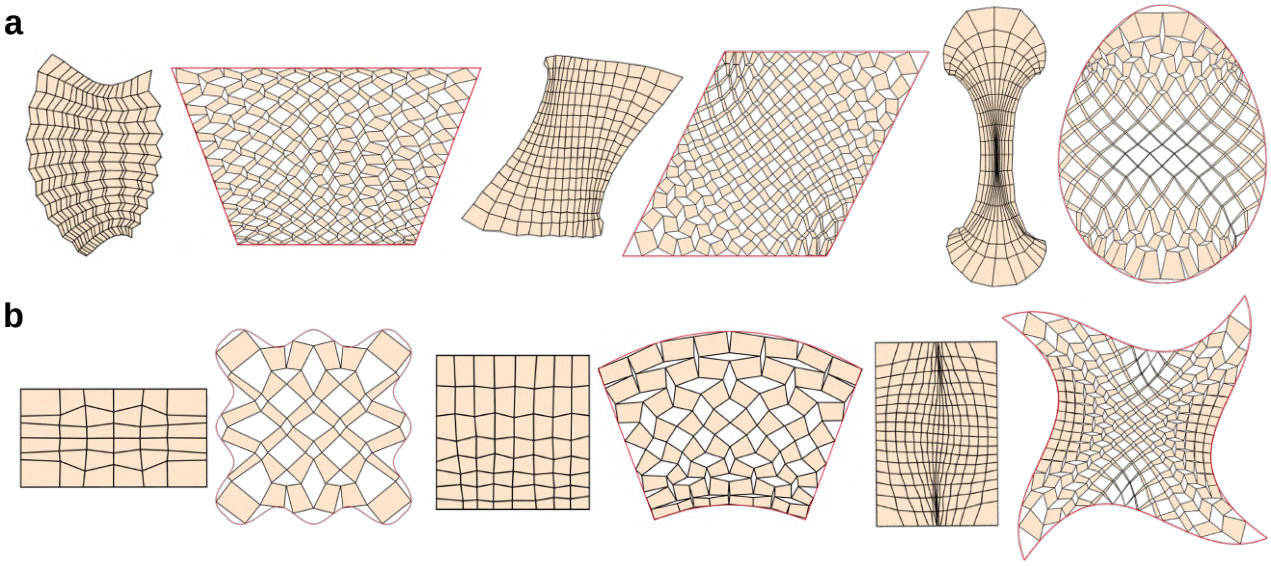

Figure S4: **Generalized quad kirigami patterns.** **a**, Generalized quad kirigami patterns with different target boundary shapes. **b**, The results with the extra constraints enforcing the pattern to be a rectangle or a square as described in Section 2.2.2.

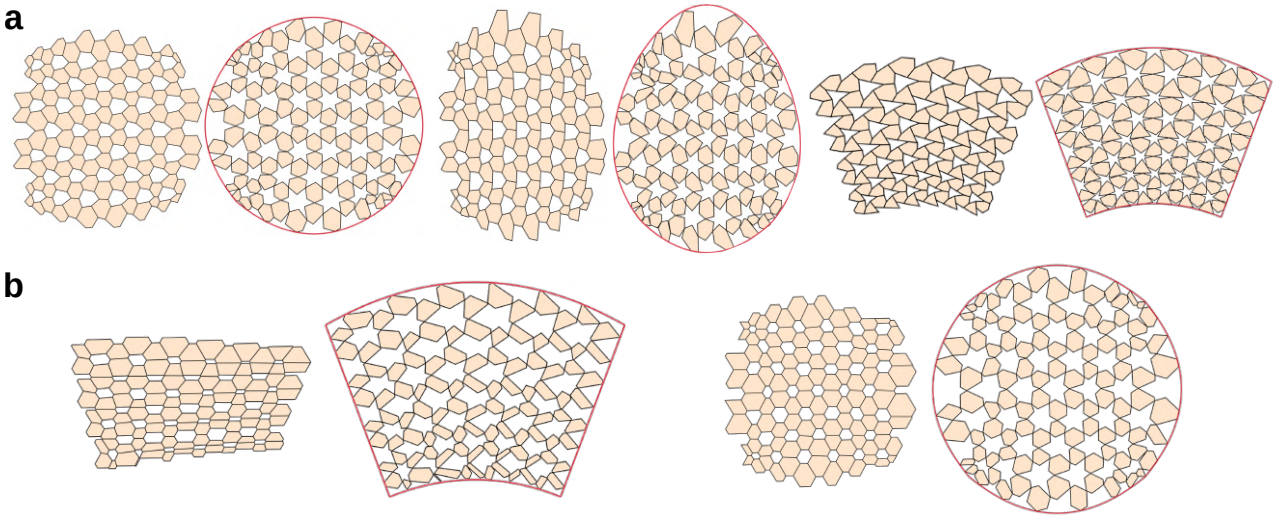

Figure S5: **Generalized hexagon kirigami patterns.** **a**, Generalized hexagon kirigami patterns with different target boundary shapes. **b**, The results with the extra regular angle constraints described in Section 2.2.3.

the standard deployed configuration. Note that all four generalized kirigami patterns obtained by the four initial guesses can be deployed to approximate the same circle, but the patterns and the deployed configurations are all different.

Figure S8 shows a fabricated model of a generalized kagome kirigami pattern obtained by our method for fitting an egg shape, produced by laser cutting a natural rubber sheet. This time, we pin the deployed state of the fabricated model and compare it with the optimization result. It can be observed that the fabrication result resembles the optimization result very well. This demonstrates the effectiveness of our inverse design method.

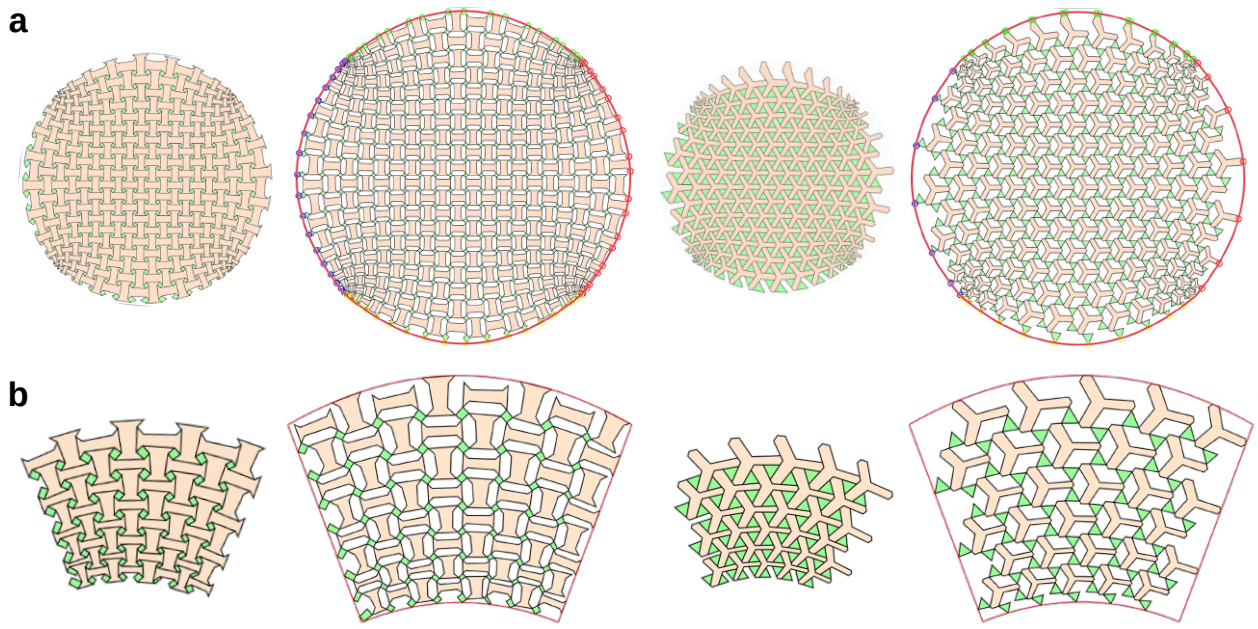

Figure S6: **Generalized multiple-cell Islamic kirigami patterns. a**, Generalized multiple-cell Islamic kirigami patterns whose deployed configurations approximate a circle. **b**, The results with the extra regular angle constraints described in Section 2.2.4.

5 Analysis of porosity and magnification factor of generalized kirigami patterns

From the results obtained by our inverse design approach, it can be observed that the generalized kirigami patterns with different types of base tessellations exhibit different properties even if their deployed configurations approximate the same shape. For instance, the size of the generalized kagome kirigami patterns changes significantly upon deployment, while the size of the generalized hexagon kirigami patterns does not change much upon deployment.

To quantitatively analyze their properties, we define the *porosity* of a generalized kirigami pattern by

$$\text{Porosity} = \frac{\text{Area of deployed configuration} - \text{Area covered by material}}{\text{Area of deployed configuration}}. \tag{S16}$$

and the *magnification factor* of a generalized kirigami pattern by

$$\text{Magnification factor} = \frac{\text{Area of deployed configuration}}{\text{Area of contracted configuration}}. \tag{S17}$$

Here, the area of a configuration is defined to be the area of the region enclosed by its boundary nodes, and the area covered by material is defined to be the total area of all faces in a pattern.

Figure S9**a**,**b** show the porosity and magnification factor of the generalized kirigami patterns that deploy and approximate different target shapes. 8 target shapes are considered for each of the triangle, quad and hexagon tessellations. An example of different patterns that deploy to approximate a rainbow shape is shown in Figure S9**c**.

Ideally, for every target shape, the area of the deployed configurations with the triangle, quad and hexagon tessellations should be as close as possible to the area of the target shape. However, it can be observed that the deployed configurations of the generalized hexagon kirigami patterns usually achieve a slightly smaller area when compared to those of the triangle and

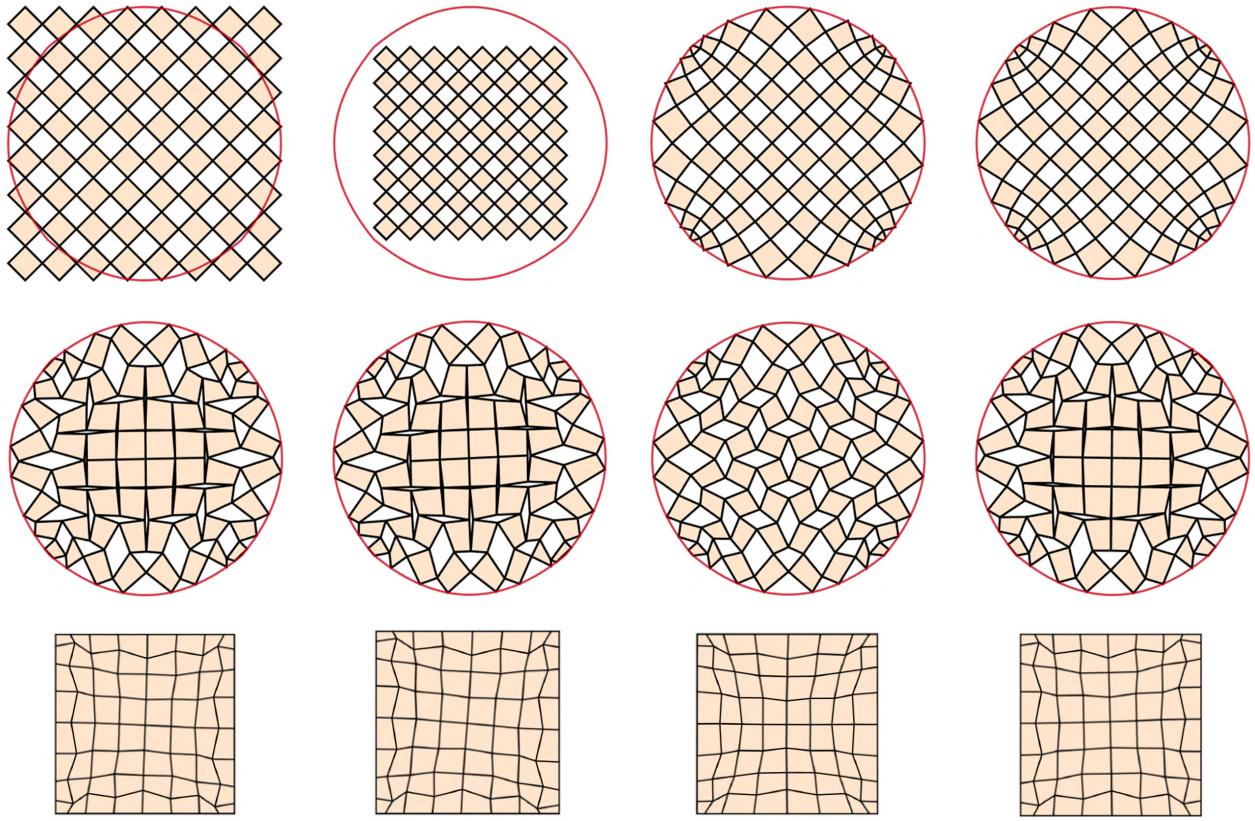

Figure S7: **An example illustrating that the generalized kirigami patterns obtained with different initial guesses can be different.** Each row shows the initial guess, the constrained optimization result, and the generalized kirigami pattern obtained. Left: The standard deployed configuration of the quad kirigami pattern. Middle left: The standard deployed configuration with rescaling. Middle right: Conformal map. Right: Quasi-conformal map.

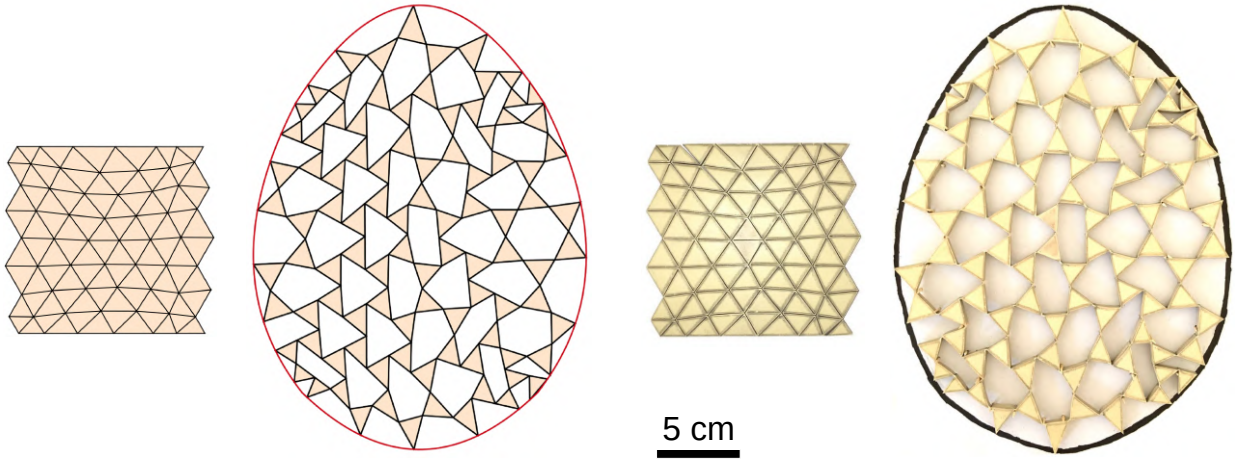

Figure S8: **A generalized kirigami pattern for fitting an egg shape with a fabricated model.** The two figures on the left show the undeployed and deployed configurations of the numerical optimization result obtained by our inverse design method. The two figures on the right show a fabricated model of the pattern and its deployed state. Pins are used to fix the position of the deployed fabricated model.

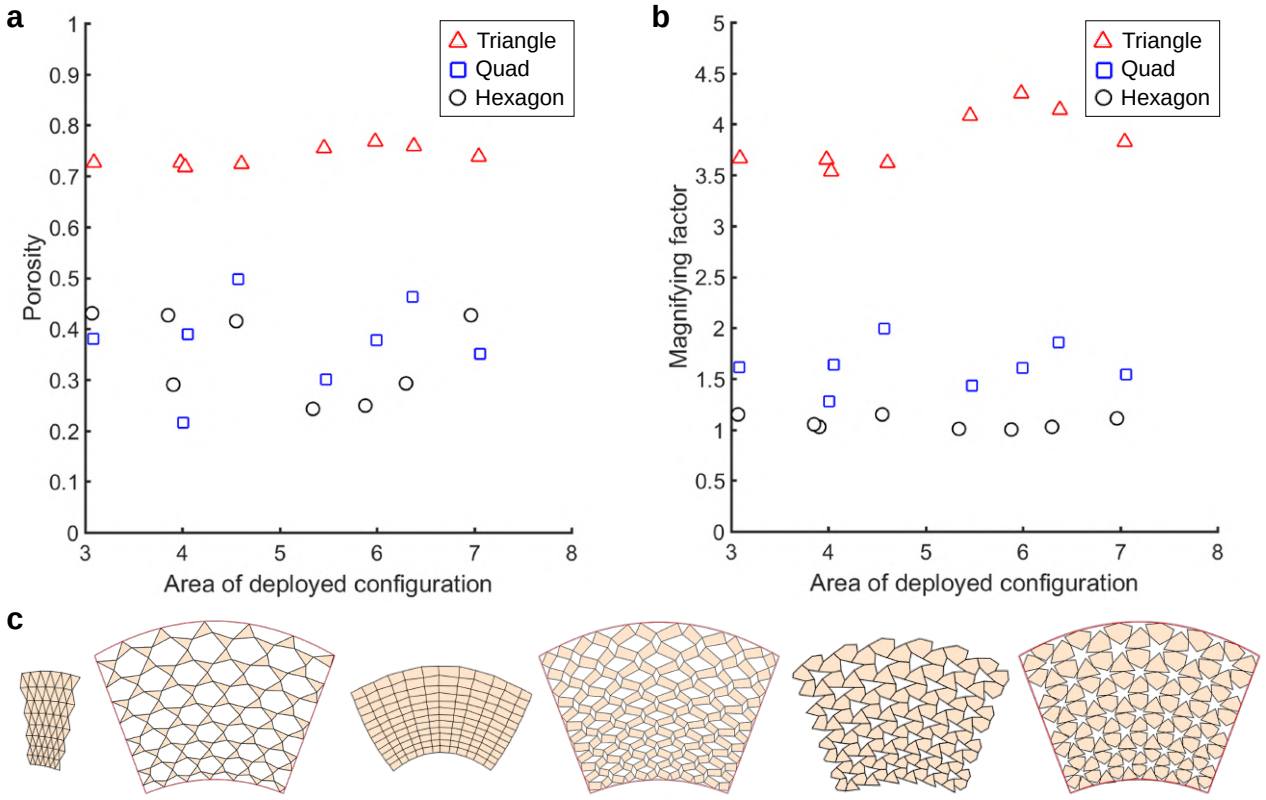

Figure S9: **Porosity and magnification factor of different generalized kirigami patterns**. **a**, The porosity of different generalized kirigami patterns. **b**, The magnification factor of different generalized kirigami patterns. **c**, Examples of the generalized triangle, quad and hexagon kirigami patterns for which the deployed configurations approximate the same boundary shape.

quad patterns. One possible reason is that hexagons are less flexible than triangles and quads in approximating shapes with higher curvature.

From the plot of porosity, it can be observed that the generalized kagome kirigami patterns achieve much higher porosity than the two other types of patterns. The porosity of the generalized quad and hex patterns are similar.

From the plot of magnification factor, it can again be observed that the generalized kagome kirigami patterns achieve much higher magnification factor than the two other types of patterns. Note that the magnification factor for the generalized hexagon patterns is close to 1, which implies that there is only a change in the shape of the hexagonal holes of the generalized hexagon kirigami patterns under deployment, while the entire shape of the patterns does not change much.

The above analysis suggests that the generalized kagome kirigami patterns are well-suited for applications that require a large change in area under deployment in order to save materials. The generalized quad kirigami patterns can be used when it is desired to achieve a moderate area change and porosity upon deployment. The generalized hexagon kirigami patterns are suitable for applications which require a change in the shape of the holes without much change in the overall area upon deployment, such as the design of a filter for allowing particles with a certain shape to pass through.

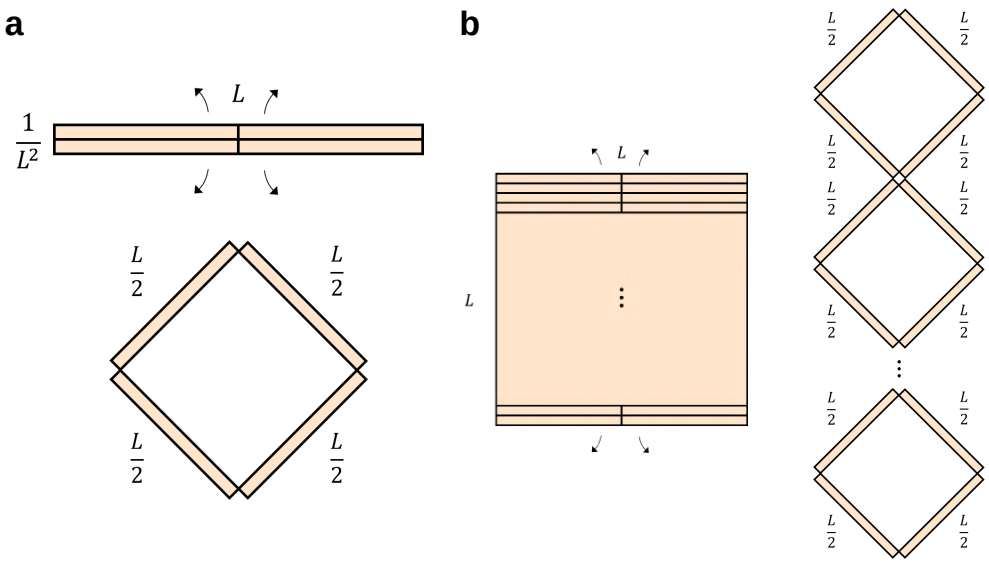

Figure S10: **Two examples of generalized quad kirigami**. **a**, A 2×2 generalized quad kirigami with width L and height $1/L^2$. **b**, A $2L^3 \times 2$ generalized quad kirigami formed by L^3 copies of the 2×2 kirigami shown in **a**.

6 Theoretical limits of the shape change of generalized kirigami patterns upon deployment

It is natural to ask about the limit of the shape change of a generalized kirigami pattern upon deployment. In this section, we study the limits for the change in area, perimeter and curvature of a planar generalized kirigami pattern upon deployment. To simplify our analysis, we focus on generalized quad kirigami patterns (i.e. the faces are all quadrilateral).

6.1 Area change upon deployment

We first study the area change Δ_{area} of a generalized kirigami pattern upon deployment, i.e.

$$\Delta_{\text{area}} = \frac{\text{Area of the deployed configuration}}{\text{Area of the contracted configuration}} - 1. \tag{S18}$$

6.1.1 Area change is unbounded if either the boundary shape of the contracted configuration or the cut topology is not fixed

We first consider the case that we are given a cut topology of the generalized kirigami (e.g. the resolution is $m \times n$) while there is no condition on the boundary shape of the contracted configuration. In this case, we can show that the area change is unbounded.

Consider a 2×2 generalized quad kirigami with width L and height $1/L^2$ as shown in Figure S10**a**. The area of the contracted configuration is $L \times 1/L^2 = 1/L$. Upon deployment, the increase in area of it is $(L/2) \times (L/2) = L^2/4$. Therefore, the area change is

$$\Delta_{\text{area}} = \frac{L^2/4}{1/L} = \frac{L^3}{4}. \tag{S19}$$

Taking $L \to \infty$, Δ_{area} tends to infinity. This shows that the area change is unbounded.

Analogously, for any other given cut topology, we can follow the construction above and obtain a generalized kirigami that achieves arbitrarily large Δ_{area} upon deployment.

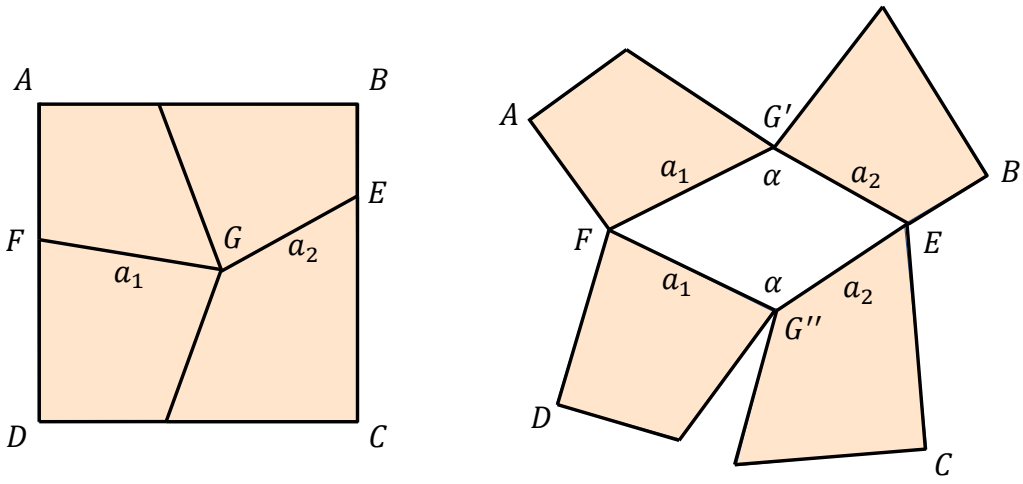

Figure S11: **A 2×2 generalized quad kirigami and its deployed configuration.**

Now consider the case that we are given the boundary shape of the contracted configuration while there is no restriction on the number of cuts to be introduced. In this case, we can again show that the area change is unbounded.

Suppose the boundary shape of the contracted configuration is required to be a perfect square with width and height L. Consider a $2L^3 \times 2$ generalized quad kirigami as shown in Figure S10**b**, which consists of L^3 copies of the 2×2 generalized quad kirigami shown in Figure S10**a**. It is easy to see that the width of the pattern is L, and the height is $\frac{1}{L^2} \times L^3 = L$. Upon deployment, each copy leads to an area increase of $L^2/4$. Therefore, we have

$$\Delta_{\text{area}} \geq \frac{(L^2/4) \times L^3}{L^2} = \frac{L^3}{4}. \tag{S20}$$

Taking $L \to \infty$, Δ_{area} also tends to infinity.

Analogously, for any other given boundary shape of the contracted configuration of a generalized kirigami pattern, we can take four points on the boundary of it as the four corners and consider a $2L^3 \times 2$ cut topology. As $L \to \infty$, we can again achieve an arbitrarily large area change upon deployment.

6.1.2 Area change is bounded if both the boundary shape of the contracted configuration and the cut topology are fixed

The analysis above suggests that we can obtain a generalized kirigami pattern that achieves arbitrary area change upon deployment by playing around with either the contracted shape or the cut topology. By contrast, it can be observed that the area change is bounded in case both of them are fixed.

As an illustration, we consider a 2×2 generalized quad kirigami for which the boundary shape of its contracted configuration is a perfect square with unit width and height (see Figure S11.

If the cut pattern is regular (i.e. the 2×2 kirigami shown in Figure S1**b**), then clearly we have

$$\Delta_{\text{area}} = \frac{5}{4} - 1 = \frac{1}{4}. \tag{S21}$$

Now suppose we relax the condition by only requiring the cuts to be vertical or horizontal (i.e. the cut pattern forms four rectangular faces but not necessarily identical squares).

Proposition 1 *For a 2×2 generalized quad kirigami with all cuts being vertical or horizontal, we have*

$$\Delta_{area} \leq \frac{1}{4}, \tag{S22}$$

where the equality holds if and only if the generalized kirigami is regular.

Proof. Using the notation in Figure S11, in this case we have $a_1 + a_2 = 1$. Note that the area of the interior hole in the deployed configuration is $a_1 a_2 \sin\alpha$. By AM-GM inequality,

$$\sqrt{a_1 a_2} \leq \frac{a_1 + a_2}{2} = \frac{1}{2} \Rightarrow a_1 a_2 \leq \frac{1}{4}, \tag{S23}$$

where the equality holds if and only if $a_1 = a_2 = 1/2$. Hence,

$$\Delta_{area} \leq \frac{1}{4}\sin\alpha \leq \frac{1}{4}. \tag{S24}$$

The equality holds if and only if $a_1 = a_2 = 1/2$ and $\alpha = \pi/2$. In other words, the equality holds if and only if the generalized kirigami is regular. ■

The above proposition suggests that among all 2×2 generalized quad kirigami patterns with only vertical and horizontal cuts, the regular one is with the greatest area change upon deployment. In fact, it can be shown that an even greater area change can be achieved if the cuts are not vertical or horizontal, but the area change is still bounded.

Proposition 2 *For a 2×2 generalized quad kirigami, we have*

$$\Delta_{area} < \frac{3}{2}. \tag{S25}$$

Proof. We refer to Figure S11 for the notation of edge lengths and angles. The area of the interior hole in the deployed configuration is given by

$$a_1 a_2 \sin\alpha \leq a_1 a_2 \leq \frac{a_1^2 + a_2^2}{2}, \tag{S26}$$

where the first equality holds if and only if $\alpha = \pi/2$, and the second equality holds if and only if $a_1 = a_2$.

Now, to find the maximum value of $a_1^2 + a_2^2$, we consider the contracted configuration and let $G = (x, y)$, $E = (1, e)$ and $F = (0, f)$. Then

$$\begin{aligned} a_1^2 + a_2^2 &= (x-1)^2 + (y-e)^2 + x^2 + (y-f)^2 \\ &= 2\left(x - \frac{1}{2}\right)^2 + \frac{1}{2} + (y-e)^2 + (y-f)^2. \end{aligned} \tag{S27}$$

Since $x, y, e, f \in [0, 1]$, we have

$$\max a_1^2 + a_2^2 = 2\left(\frac{1}{2}\right)^2 + \frac{1}{2} + 1 + 1 = 3, \tag{S28}$$

where the maximum is attained if and only if $(x, y, e, f) = (0, 1, 0, 0)$, $(0, 0, 1, 1)$, $(1, 1, 0, 0)$ or $(1, 0, 1, 1)$. As the cut pattern that we consider is non-degenerate, none of the four solutions above can be achieved in the contracted configuration. Therefore, we have

$$\Delta_{area} \leq \frac{a_1^2 + a_2^2}{2} < \frac{3}{2}. \tag{S29}$$

■

The above analysis shows that the area change of a 2×2 generalized quad kirigami with prescribed contracted shape upon deployment is always bounded regardless of its cut geometry. Analogously, for any other given cut topology and boundary shape of the contracted configuration, the above approach can be used to prove that the area change upon deployment is bounded.

6.2 Perimeter change upon deployment

We then study the perimeter change of a generalized kirigami pattern upon deployment:

$$\Delta_{\text{perimeter}} = \frac{\text{Perimeter of the deployed configuration}}{\text{Perimeter of the contracted configuration}} - 1. \tag{S30}$$

6.2.1 Perimeter change is unbounded if the cut topology is not fixed

Suppose we are given the boundary shape of the contracted configuration of a generalized kirigami pattern, while there is no restriction on the number of cuts to be introduced. In this case, we can show that the perimeter change is unbounded.

We consider the example shown in Figure S10**b**. For this example, note that the boundary of the deployed configuration consists of $4L^3$ segments with length $\frac{L}{2}$ and $4L^3+4$ segments with length $\frac{1}{2L^2}$. Therefore, we have

$$\Delta_{\text{perimeter}} = \frac{4L^3 \cdot \frac{L}{2} + (4L^3+4) \cdot \frac{1}{2L^2}}{4L} - 1 = L^3 + \frac{1}{L^3}. \tag{S31}$$

Taking $L \to \infty$, we have $\Delta_{\text{perimeter}} \to \infty$.

Analogous to the study of area change, by suitably modifying the above example, it is easy to see that the perimeter change is unbounded for any given boundary shape of the contracted configuration as long as the cut topology is not fixed.

6.2.2 Perimeter change is bounded if the cut topology is fixed

Now suppose the cut topology of the generalized kirigami pattern is fixed (e.g. the resolution of it is $m \times n$). In this case, we can show that the perimeter change of the generalized kirigami upon deployment is always bounded.

Let p be the perimeter of the contracted configuration of a generalized kirigami. Let d be the diameter of the smallest circle which circumscribes the contracted configuration. It is easy to see that $d \leq p$.

As the resolution is $m \times n$, there are at most $2(m-1)+2(n-1) = 2m+2n-4$ new boundary edges upon deployment, and each of them must be with length not greater than d. Hence, we have

$$\Delta_{\text{perimeter}} \leq \frac{p + (2m+2n-4)d}{p} - 1 = \frac{(2m+2n-4)d}{p} \leq 2m+2n-4. \tag{S32}$$

This shows that the perimeter change is bounded with a fixed cut topology.

6.3 Curvature change upon deployment

Finally, we study the curvature change of generalized kirigami patterns upon deployment. Here, the curvature is defined by smoothly connecting the nodes in the deployed configuration which correspond to the boundary codes in the contracted configuration (i.e. the nodes at the zig-zag parts near the deployed boundary are not taken into account).

6.3.1 Curvature change is unbounded if the cut topology is not fixed

The example shown in Figure S10**b** suggests that a target shape with very highly curved parts can be approximated by a generalized kirigami even if the boundary shape of the contacted configuration is fixed, and hence the curvature change upon deployment is unbounded.

6.3.2 Curvature change is bounded if the cut topology is fixed

It is well known that for any smooth simple closed plane curve C, the total curvature is 2π:

$$\int_C k(s)ds = 2\pi. \tag{S33}$$

For the case that the cut topology is fixed, let C be the boundary of a deployed configuration. We have already shown that the perimeter change is bounded in this case, and hence the length of C is bounded. From the above total curvature formula, the curvature change is also bounded.

7 Generalized kirigami patterns for surface fitting

As discussed in the main text, we can extend our inverse design approach for producing generalized kirigami patterns whose deployed configuration approximate a prescribed surface.

In the main text, we presented an analysis on the curvature at the holes of the deployed configurations of generalized quad kirigami patterns. Here, we describe the technical details of the analysis. Suppose $\mathbf{p}_1, \mathbf{p}_2, \mathbf{p}_3, \mathbf{p}_4$ are the four vertices in anti-clockwise orientation of a hole in the deployed configurations. To study the curvature residing at the hole, we consider fitting the hole by a smooth surface. In particular, the surface should be compatible with all the adjacent quads along the straight edges. A suitable candidate for such surface is the bicubic Bézier surface [4] in the form

$$\mathbf{X}(u,v) = \sum_{i=0}^{3}\sum_{j=0}^{3} B_i^3(u)B_j^3(v)\mathbf{k}_{i,j}, \tag{S34}$$

where $u, v \in [0,1]$. Here, $\mathbf{k}_{i,j}$ are 16 control points including the four vertices $\mathbf{k}_{0,0} = \mathbf{p}_1$, $\mathbf{k}_{3,0} = \mathbf{p}_2$, $\mathbf{k}_{3,3} = \mathbf{p}_3$, $\mathbf{k}_{0,3} = \mathbf{p}_4$, and the remaining control points are

$$\begin{aligned}
\mathbf{k}_{1,0} &= \frac{2\mathbf{k}_{0,0}+\mathbf{k}_{3,0}}{3}, \mathbf{k}_{2,0} = \frac{\mathbf{k}_{0,0}+2\mathbf{k}_{3,0}}{3}, \mathbf{k}_{1,3} = \frac{2\mathbf{k}_{0,3}+\mathbf{k}_{3,3}}{3}, \mathbf{k}_{2,3} = \frac{\mathbf{k}_{0,3}+2\mathbf{k}_{3,3}}{3},\\
\mathbf{k}_{0,1} &= \frac{2\mathbf{k}_{0,0}+\mathbf{k}_{0,3}}{3}, \mathbf{k}_{0,2} = \frac{\mathbf{k}_{0,1}+2\mathbf{k}_{0,3}}{3}, \mathbf{k}_{3,1} = \frac{2\mathbf{k}_{3,0}+\mathbf{k}_{3,3}}{3}, \mathbf{k}_{3,2} = \frac{\mathbf{k}_{3,0}+2\mathbf{k}_{3,3}}{3},\\
\mathbf{k}_{1,1} &= \frac{2\mathbf{k}_{1,0}+\mathbf{k}_{1,3}}{3}, \mathbf{k}_{1,2} = \frac{\mathbf{k}_{1,0}+2\mathbf{k}_{1,3}}{3}, \mathbf{k}_{2,1} = \frac{2\mathbf{k}_{2,0}+\mathbf{k}_{2,3}}{3}, \mathbf{k}_{2,2} = \frac{\mathbf{k}_{2,0}+2\mathbf{k}_{2,3}}{3}.
\end{aligned} \tag{S35}$$

$B_0^3, B_1^3, B_2^3, B_3^3$ are the Bernstein polynomials of degree 3 given by

$$B_i^3(u) = \binom{3}{i} u^i(1-u)^{3-i}. \tag{S36}$$

The boundary of the Bézier surface is given by $\{\mathbf{X}(u,v) : u, v = 0, 1\}$. As there are four collinear control points on each boundary edge of the hole, the Bézier surface will pass through all the edges exactly, making the surface compatible with all the surrounding quads. The surface is planar if and only if the four vertices of the hole are coplanar.

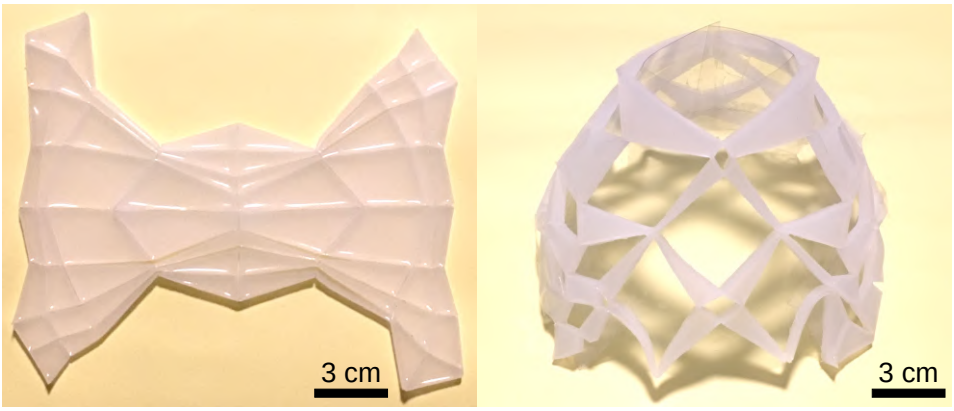

Figure S12: **A physical model of the generalized quad pattern shown in Figure 4d in the main text fabricated using PDMS.** The model achieves a significant shape change and fits a hat-like surface (the underlying transparent sheet) upon deployment.

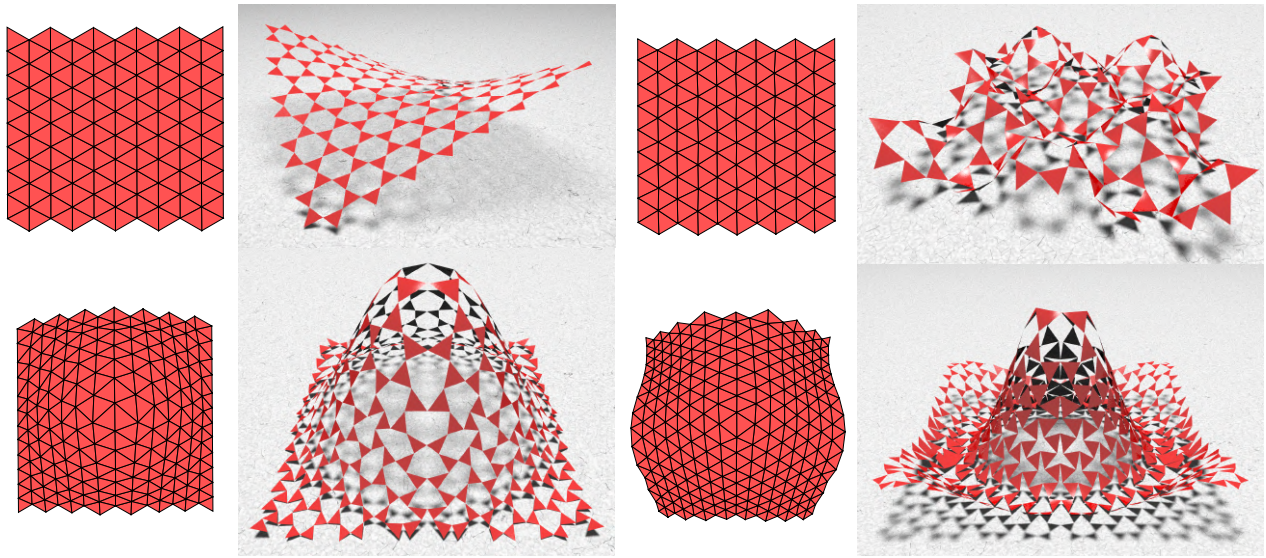

Figure S13: **Generalized kagome kirigami patterns for surface fitting.** The target surfaces are respectively a hyperbolic paraboloid, a landscape surface with multiple peaks, a bivariate Gaussian and a Mexican hat. For each target surface, the resulting generalized kirigami pattern and its deployed configuration are shown. It can be observed that our approach is capable of controlling the boundaries and the shape of the triangular faces of the generalized kirigami patterns for approximating different surfaces.

The mean curvature and the Gauss curvature at every hole are then given by

$$H(u,v) = \frac{eG - 2fF + gE}{2(EG - F^2)} \tag{S37}$$

and

$$K(u,v) = \frac{eg - f^2}{EG - F^2}, \tag{S38}$$

where $E = \langle \mathbf{X}_u, \mathbf{X}_u \rangle$, $F = \langle \mathbf{X}_u, \mathbf{X}_v \rangle$, $G = \langle \mathbf{X}_v, \mathbf{X}_v \rangle$, $e = \langle \mathbf{N}, \mathbf{X}_{uu} \rangle$, $f = \langle \mathbf{N}, \mathbf{X}_{uv} \rangle$, $g = \langle \mathbf{N}, \mathbf{X}_{vv} \rangle$, and $\mathbf{N}$ is the outward unit normal of the Bézier surface.

Figure S12 shows a physical model of a generalized quad kirigami pattern for surface fitting fabricated using Polydimethylsiloxane (PDMS). A mold is first 3D printed to form a negative

space of the undeployed pattern. Then, PDMS is poured into the mold, thereby creating a deployable kirigami structure. It can be observed that the deployed shape fits a hat-like surface very well. This shows that our inverse kirigami design is applicable to different materials.

Besides the generalized quad kirigami patterns shown in the main text, we can also consider generalizing the kagome kirigami patterns for surface fitting. The formulation is almost identical to the case of quad pattern, except for that the planarity constraints are automatically satisfied for the case of triangles. Figure S13 shows the surface fitting results with generalized kagome kirigami patterns produced by our method. Again, our approach is capable of fitting surfaces with different curvature properties, and further satisfying additional boundary constraints of the generalized kirigami patterns.

References

[1] Rafsanjani, A., & Pasini, D.. Bistable auxetic mechanical metamaterials inspired by ancient geometric motifs. Extreme Mechanics Letters **9**, 291-296 (2016).

[2] Choi, G. P. T., & Lui, L. M.. A linear formulation for disk conformal parameterization of simply-connected open surfaces. Advances in Computational Mathematics **44(1)**, 87-114 (2018).

[3] Meng, T. W., Choi, G. P. T., & Lui, L. M.. TEMPO: feature-endowed Teichmüller extremal mappings of point clouds. SIAM Journal on Imaging Sciences **9(4)**, 1922-1962 (2016).

[4] Farin, G.E., & Farin, G.. Curves and surfaces for CAGD: a practical guide. Morgan Kaufmann (2002).